

Wavelength division multiplexing large-aperture multi-order differential metasurface calculator

Liming Wei(魏黎明), Anting Gao(高安廷), Junfeng Li(李俊锋), Wenke Lan(兰文科), Xilong Liu(刘喜龙), and Yikai Chen(陈漪恺)

Citation: Chin. Phys. B, 2026, 35 (**6**): 067802. DOI: 10.1088/1674-1056/ae067d
http://cpb.iphy.ac.cn; http://iopscience.iop.org/cpb

What follows is a list of articles you may be interested in

Tunable multi-frequency exceptional points in non-Hermitian terahertz metasurfaces

Xiang Hou(侯翔), Fangze Deng(邓方泽), Zhihua Han(韩志华), Yumeng Ma(马宇萌), Chenglong Wang(王成龙), Yuchao Li(李玉超), Keke Cheng(程可可), Ke Ma(马克), Yansheng Shao(邵延胜), Ruidan Zhou(周瑞丹), Yuping Zhang(张玉萍), Meng Liu(刘蒙), and Huiyun Zhang(张会云)
Chin. Phys. B, 2026, 35 (**5**): 057802. DOI: 10.1088/1674-1056/ae12d8

Topological edge state coupled mode-induced tetra-band tunable spin-dependent perfect absorption

Ji-Peng Wu(伍计鹏), Xi-Rui Zeng(曾玺瑞), Yu-Lei Liao(廖煜磊), Rong-Zhou Zeng(曾荣周), Hong Wen(文鸿), Xiao-Yu Dai(戴小玉), and Yuan-Jiang Xiang(项元江)
Chin. Phys. B, 2026, 35 (**4**): 047801. DOI: 10.1088/1674-1056/ae00b2

Multifunctional light-field modulation based on hybrid nonlinear metasurfaces

Shuhang Qian(钱树航), Kai Wang(王凯), Jiaxing Yang(杨加兴), Chao Guan(关超), Hua Long(龙华), and Peixiang Lu(陆培祥)
Chin. Phys. B, 2023, 32 (**10**): 107803. DOI: 10.1088/1674-1056/acdc13

Designing radiative cooling metamaterials for passive thermal management by particle swarm optimization

Shenshen Yan(闫申申), Yan Liu(刘岩), Zi Wang(王子), Xiaohua Lan(兰晓华), Yi Wang(汪毅), and Jie Ren(任捷)
Chin. Phys. B, 2023, 32 (**5**): 057802. DOI: 10.1088/1674-1056/acc061

Graphene metasurface-based switchable terahertz half-/quarter-wave plate with a broad bandwidth

Xiaoqing Luo(罗小青), Juan Luo(罗娟), Fangrong Hu(胡放荣), and Guangyuan Li(李光元)
Chin. Phys. B, 2023, 32 (**2**): 027801. DOI: 10.1088/1674-1056/ac80a8

Wavelength division multiplexing large-aperture multi-order differential metasurface calculator

Liming Wei(魏黎明)[1,2], Anting Gao(高安廷)[1,2], Junfeng Li(李俊锋)[1,2], Wenke Lan(兰文科)[1,2], Xilong Liu(刘喜龙)[1,2], and Yikai Chen(陈漪恺)[1,2,†]

[1] *Department of Information Physics and Engineering, Nanjing University of Science and Technology, Nanjing* 210094, *China*
[2] *Engineering Research Center of Semiconductor Device Optoelectronic Hybrid Integration in Jiangsu Province, Nanjing* 210094, *China*

(Received 16 July 2025; revised manuscript received 3 September 2025; accepted manuscript online 15 September 2025)

Optical differentiation is crucial for high-speed image processing, but most optical analog spatial differentiators based on metasurfaces are currently limited to a single type of low-order differentiation operation. We present a dielectric metasurface composed of silicon hollow cylinders that leverages electric quadrupole (EQD) and magnetic dipole (MD) resonances to achieve wavelength-tunable two-dimensional (2D) multi-order differentiation. Specifically, at 1340 nm (MD-dominant), 1140 nm (hybrid EQD–MD), and 1010 nm (EQD-dominant), the metasurface performs second-, fourth-, and sixth-order differentiations, respectively. The device features a 430-nm bandwidth, a maximum numerical aperture of 0.71, and a maximum transmittance of 96%, enabling high-quality edge extraction for complex images. We believe this to be the first integration of wavelength-division multiplexing and multi-order differentiation in a single-layer metasurface, advancing compact and multifunctional optical computing for applications such as autonomous driving and medical imaging.

Keywords: optical differential calculation, wavelength division multiplexing, dielectric metasurface

PACS: 78.67.Pt, 42.79.Hp, 42.30.Kq, 42.30.Va

DOI: 10.1088/1674-1056/ae067d **CSTR:** 32038.14.CPB.ae067d

1. Introduction

Optical computing holds significant advantages over electronic computing, such as high speed, parallel processing, low power consumption, broad bandwidth, and strong resistance to interference.[1–3] Optical differentiation,[4,5] a key technology, can directly perform differentiation in the optical domain, enabling rapid edge feature extraction of targets.[6,7] It has great application value in fields like autonomous driving, medical imaging, and AR/VR.[8–10]

Traditional optical computing[11] systems mainly use 4F systems[12,13] composed of double lens groups and spatial filters. However, the large volume of optical components in this design results in an oversized system, failing to meet the demands of modern miniaturized devices.[14] With the development of metasurface technology, this situation has been greatly improved. Metasurfaces,[15] with their subwavelength structural characteristics, offer a promising approach for compact optical computing systems. Researchers have implemented differentiation functions on metasurface platforms using various mechanisms, such as surface plasmon polariton resonance,[16–18] half-wave plate interference effects,[19] and the photonic spin Hall effect.[20,21] Yet, these methods generally have two limitations: they can only achieve one-dimensional (1D) or low-order differentiation and struggle to ensure high-order differentiation performance.

As research has advanced, numerous novel resonance mechanisms have been applied to the design of metasurface differentiators, such as guided-mode resonance,[22] toroidal dipole resonance,[23] magnetic resonance,[24] waveguide grating modes,[25] and quasi-guided wave states[26–29] in photonic crystals. While these technologies have achieved 2D second-order differentiation,[30] they have notable drawbacks: limited operating wavelength ranges, a single differentiation function per device, and low numerical aperture causing poor spatial resolution. These bottlenecks hinder the practical efficiency and industrialization of current metasurface differentiators.

In this paper, we present an innovative single-layer dielectric metasurface[31] based on electric quadrupole (EQD) and magnetic dipole (MD) resonances, achieving wave-multiplexed[32,33] multi-order differentiation in transmission mode. The EQD resonance, with its complex field distribution, offers greater design flexibility, while the MD resonance enhances energy storage efficiency through low scattering loss and a high Q-factor.[34] By precisely tuning geometry of silicon hollow cylinders, the metasurface performs 2D second-, fourth-, and sixth-order differentiations at 1340 nm, 1140 nm, and 1010 nm, respectively. It has an operating bandwidth of 430 nm, and at the operating wavelength of 1340 nm, the numerical aperture (NA) reaches a maximum value of 0.71, enabling a theoretical limit resolution of 1.1 μm. This breakthrough paves a new path for optical computing, autonomous driving, and biomedical imaging.

†Corresponding author. E-mail: ykchen@njust.edu.cn

© 2026 Chinese Physical Society and IOP Publishing Ltd. All rights, including for text and data mining, AI training, and similar technologies, are reserved.

2. Simulations and design

Figure 1 illustrates the fundamental operating principle of the silicon hollow-cylinder metasurface for optical differentiation. A 2D image with the characters "NJUST" serves as the input signal, modulating the incident plane wave: white areas permit direct light transmission, while black areas block it entirely. Upon encountering high-contrast image edges, significant diffraction occurs, producing large-angle wavevector components. By leveraging the nonlocal (wavevector-dependent) response of a cleverly designed metasurface, the incident optical field is directly modulated in the spatial frequency domain to achieve specific spatial-domain differential computation functions. The unit period of the metasurface is smaller than the operating wavelength, so its field distribution is concentrated near the units, and the coupling between units occurs only through near-field interactions. This Green's function method[13] directly filters the frequency-domain components in real space, eliminating the need for the far-field Fourier transform process using lenses and thus avoiding reliance on a 4F system. The metasurface's spatial dispersion properties allow these large-angle components to transmit efficiently while suppressing small-angle components, performing spatial differentiation and edge feature extraction on the input image. Central to this process is the precise control of the metasurface's optical transfer function, the detailed design of which will be elaborated in the subsequent text.

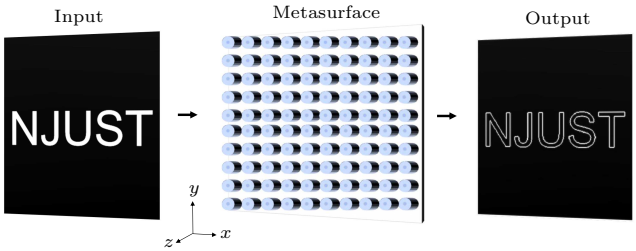


Fig. 1. Schematic illustration of the edge detection of the 2D optical differentiator using the metasurface.

In real space, performing a 2D n-th order differentiation on the input optical field physically means executing n-th order partial differentiation operations along the x and y directions respectively and then superimposing the results, with the mathematical expression as follows:[35]

$$\boldsymbol{E}_{\text{out}}(x,y) = \left(\frac{\partial^n}{\partial x^n} + \frac{\partial^n}{\partial y^n}\right)\boldsymbol{E}_{\text{in}}(x,y), \tag{1}$$

where $\boldsymbol{E}_{\text{out}}(x,y)$ denotes the output optical field after differentiation, and $\partial^n/\partial x^n$ and $\partial^n/\partial y^n$ represent the n-th order partial derivatives in the x and y directions, respectively.

In the Fourier domain, for any function $f(x,y)$, the Fourier transform of its n-th order partial derivative satisfies

$$\mathcal{F}\left\{\frac{\partial^n f(x,y)}{\partial x^n}\right\} = (\mathrm{i}k_x)^n \cdot \tilde{f}(k_x,k_y), \tag{2}$$

$$\mathcal{F}\left\{\frac{\partial^n f(x,y)}{\partial y^n}\right\} = (\mathrm{i}ky)^n \cdot \tilde{f}(k_x,k_y), \tag{3}$$

where $\mathcal{F}\{\cdot\}$ denotes the 2D Fourier transform, $\tilde{f}(k_x,k_y)$ is the frequency–domain representation of $f(x,y)$, $k_x = (2\pi/\lambda)\sin\theta\cos\phi$ and $k_y = (2\pi/\lambda)\sin\theta\sin\phi$ are the in-plane wave vectors, λ is the wavelength, θ is the incident angle, ϕ is the azimuthal angle, and i is the imaginary unit.

By performing the Fourier transform on both sides of Eq. (1) and combining it with the linearity of the Fourier transform, we can obtain

$$E_{\text{out}}(k_x,k_y) = \mathcal{F}\left\{\frac{\partial^n E_{\text{in}}(x,y)}{\partial x^n} + \frac{\partial^n E_{\text{in}}(x,y)}{\partial y^n}\right\}. \tag{4}$$

Substituting the derivative transformation properties of Eqs. (2) and (3), equation (4) can be rewritten as

$$E_{\text{out}}(k_x,k_y) = [(\mathrm{i}k_x)^n + (\mathrm{i}k_y)^n] \cdot E_{\text{in}}(k_x,k_y). \tag{5}$$

The optical transfer function (OTF) is the ratio of the output optical field to the input optical field in the frequency domain; thus, from Eq. (5), we have

$$H(k_x,k_y) = \frac{E_{\text{out}}(k_x,k_y)}{E_{\text{in}}(k_x,k_y)} = (\mathrm{i}k_x)^n + (\mathrm{i}k_y)^n. \tag{6}$$

For isotropic differentiation, the OTF should depend only on the magnitude of the in-plane wave vector and be independent of the azimuthal angle ϕ. Therefore, the OTF for isotropic n-th order differentiation is finally expressed as[36]

$$H(k_{xy}) = (\mathrm{i}k_{xy})^n, \tag{7}$$

where $k_{xy} = k\sin\theta$, k is the incident wave vector, and θ is the angle of incidence of the light wave. This implies that the transmittance of the metasurface should be zero at normal incidence, and the transmittance should increase as the incidence angle changes from normal to oblique, with the transmittance increasing as the angle of incidence increases.

Our target metasurface is designed to remove low-frequency components in k-space and allow high-frequency components to be transmitted according to the rules mentioned above, thereby exhibiting high-pass filtering capabilities. To design such a metasurface, we carried out numerical studies using the finite-difference time-domain (FDTD) method. The metasurface consists of silicon hollow cylinders on a glass substrate. The silicon hollow cylinders have an outer diameter D of 400 nm, an inner diameter d of 124 nm, a height H of 450 nm, and the unit cell has a period P of 600 nm, as shown in Fig. 2(a). We calculated the transmission spectrum response of the metasurface under normal incidence for the near-infrared spectral range from 900 nm to 1600 nm, with p-polarized incident light, as shown in Fig. 2(b). It can be observed that the transmission is below 0.1 for the wavelength range from 970 nm to 1400 nm, with near-zero transmission at the resonant wavelengths of 1010 nm, 1140 nm, and 1340 nm. To understand the nature of the resonances at different wavelengths,

we performed an analysis using multipole decomposition techniques, and the results are shown in Fig. 2(c). It can be clearly seen that at the resonant wavelength of 1010 nm, the electric quadrupole (EQD) resonance dominates. As the wavelength increases, this resonance mode gradually weakens, while the magnetic dipole (MD) resonance gradually strengthens. At the resonant wavelength of 1140 nm, a mixed resonance of electric quadrupole resonance (EQD) and magnetic dipole resonance (MD) appears, and at the resonant wavelength of 1340 nm, the magnetic dipole resonance (MD) dominates.

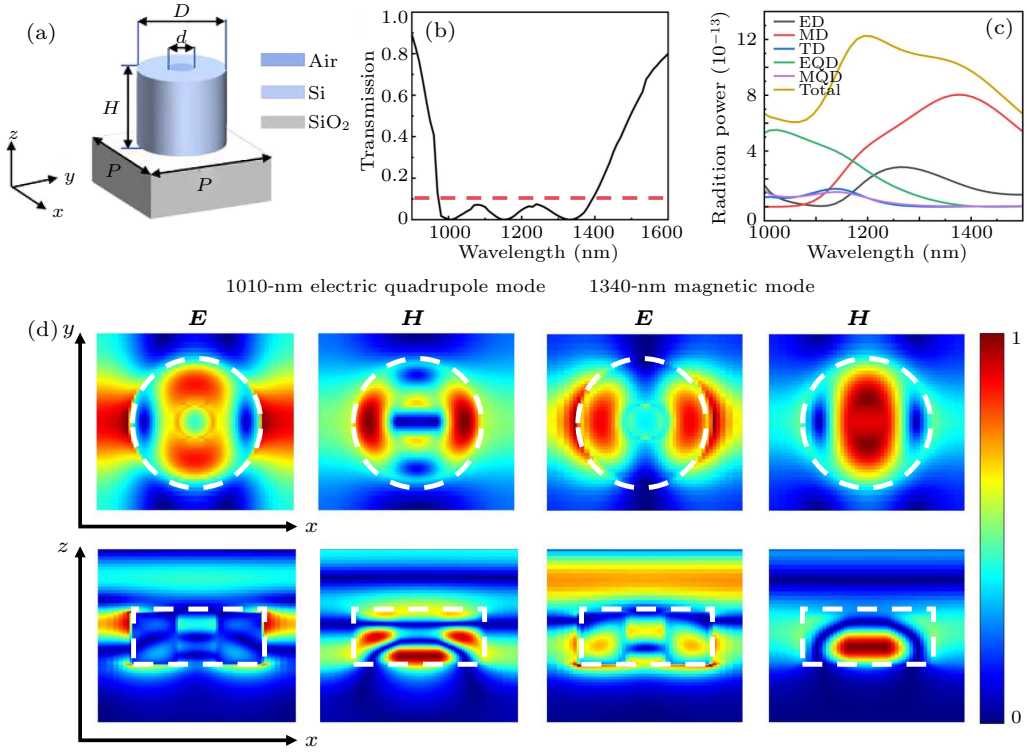


Fig. 2. Parameters and resonance characteristics of the silicon hollow cylinder metasurface. (a) Schematic diagram of the silicon hollow cylinder unit cell. (b) Transmission spectrum of the metasurface for p-polarized light, with the red dashed line indicating the $T = 0.1$ threshold. (c) Multipole decomposition of the metasurface. (d) Electromagnetic field distributions at the resonant wavelengths of 1010 nm and 1340 nm.

To gain an intuitive understanding of the resonant behavior of the silicon hollow cylinder metasurface, we analyzed the electromagnetic field distributions in the *x*–*y* and *x*–*z* planes of the unit cell at the resonant wavelengths of 1010 nm and 1340 nm under normal incidence, as shown in Fig. 2(d). At 1010 nm, the electric field (*E*) distribution in the *x*–*y* plane exhibits a typical quadrupole symmetry, with four high-intensity regions along the *x* and *y* axes, consistent with the characteristics of electric quadrupole (EQD) resonance. At 1340 nm, the magnetic field (*M*) distribution in the *x*–*y* plane shows two high-intensity regions along the *y* axis, which are significantly enhanced and dominant, aligning with the features of magnetic dipole (MD) resonance. These results confirm that the primary multipolar contributors to the resonance effects are EQD and MD resonances.

3. Methods

To determine the precise dependence of the transmission on the incidence angle of the silicon hollow cylinder metasurface under p-polarization, we calculated the transmission spectra and phase relationships of the metasurface at the resonant wavelength of 1340 nm for incidence angles ranging from $-45°$ to $45°$, as shown in Figs. 3(a) and 3(d). The transmission (black solid line) increases significantly with the incidence angle, resembling a parabolic shape. Meanwhile, the phase of the metasurface remains largely stable (with fluctuations between 0 and 0.5 rad) across different oblique incidence angles from $-45°$ to $45°$, providing the necessary conditions for second-order differentiation. Notably, the maximum incidence angle reaches $45°$, corresponding to a numerical aperture (NA) of approximately 0.71. This bandwidth allows for an edge detection theoretical limit resolution as high as 1.1 μm ($0.61 \cdot \lambda/\mathrm{NA}$), equivalent to 0.86λ). At $\theta = \pm 45°$, the maximum transmission is about 96%. Such a large NA and high transmittance help obtain extra information about the incident light field, enabling high spatial resolution beyond the wavelength scale. For comparison, the ideal transfer function for second-order differentiation (red dashed line) is also provided, and the two results are nearly identical.

To verify the capability of the metasurface for implementing 2D second-order differentiation under p-polarized light, we characterized the transmission characteristics and phase of the incident light at a wavelength of 1340 nm across different azimuthal angles, with the results presented in Figs. 3(e) and

3(h).

The transmission optical transfer function (OTF) in Fig. 3(e) shows that across all tested azimuthal angles, the transmittance remains close to 0 at small incident angles and gradually approaches 100% as the incident angle increases. This frequency-selective property suppresses the low-frequency components of the incident light while enabling the transmission of high-frequency components within the incident angle range of $-45°$ to $45°$, thus providing support for 2D second-order differential operations. Notably, there are partial deviations in transmission amplitude between the diagonal directions and the x- and y-directions; however, these deviations do not impair the differential operation capability, as detailed in the subsequent image calculation results. In addition, the transmitted phase results in Fig. 3(h) indicate that within the designed incident angle range, the transmitted phase exhibits minimal variation for all in-plane wave vectors. This stable phase response, combined with the aforementioned frequency-selective transmission property, confirms that the silicon hollow-cylinder metasurface meets the requirements for implementing 2D second-order differentiation under p-polarized light at a wavelength of 1340 nm.

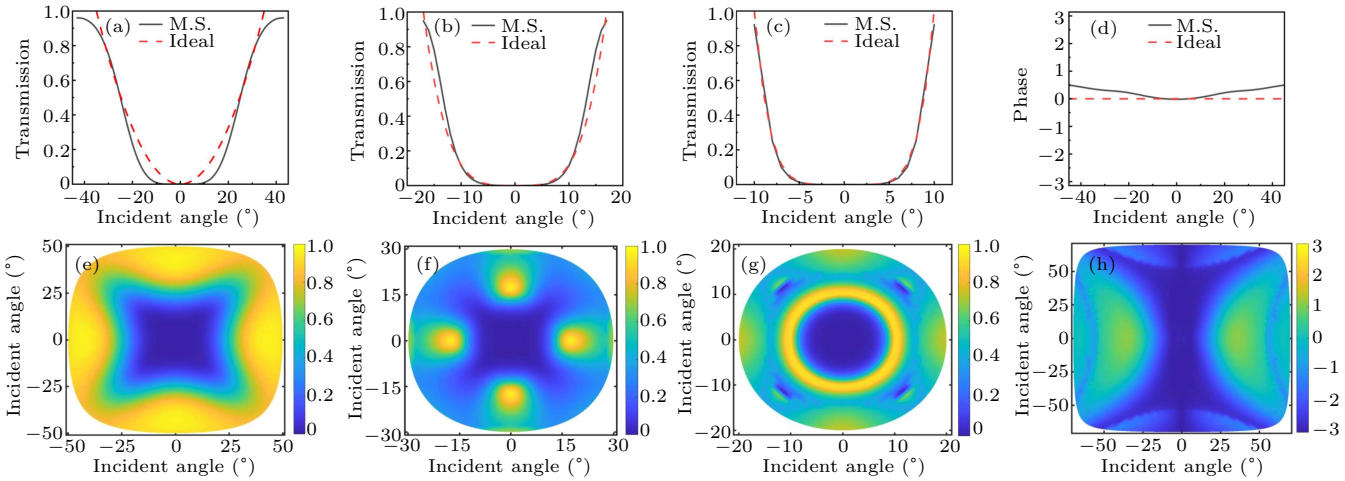


Fig. 3. The 1D and 2D optical transfer functions (OTFs) and phase distributions of the silicon hollow cylinder metasurface. (a) OTF along the x-direction at 1340 nm for the metasurface (black solid line) and the ideal second-order differentiation (red dashed line). (b) OTF along the x-direction at 1140 nm for the metasurface and the ideal fourth-order differentiation. (c) OTF along the x-direction at 1010 nm for the metasurface and the ideal sixth-order differentiation. (d) Phase distribution along the x-direction at 1340 nm for the metasurface and the ideal case. (e)–(g) 2D OTFs at 1340 nm, 1140 nm, and 1010 nm. (h) 2D phase distribution at 1340 nm.

We also calculated the transmission spectra of the metasurface at the resonant wavelength of 1140 nm for incidence angles ranging from $-20°$ to $20°$, as shown in Figs. 3(b) and 3(f). We can see that the transmission curve almost perfectly matches the ideal transfer function for fourth-order differentiation (red dashed line). The maximum incidence angle here is $18°$, corresponding to a numerical aperture (NA) of approximately 0.31. At $\theta = \pm 18°$, the maximum transmittance is about 95%. At this point, the metasurface's 2D spatial dispersion transmission remains insensitive to the azimuth angles in the x and y directions. This shows that the silicon hollow cylinder metasurface can perform 2D fourth-order differentiation at the working wavelength of 1140 nm.

Similarly, we calculated the transmission spectra of the metasurface at the resonant wavelength of 1010 nm for incidence angles between $-15°$ and $15°$, as displayed in Figs. 3(c) and 3(g). The transmission curve here almost exactly matches the ideal transfer function for sixth-order differentiation (red dashed line). The maximum incidence angle is $10°$, with a corresponding NA of around 0.17. At $\theta = \pm 11°$, the maximum transmission is approximately 92%. Moreover, the 2D spatial dispersion transmission of the metasurface now shows an almost circular contour, indicating insensitivity to the azimuth. Thus, the silicon hollow cylinder metasurface is capable of performing 2D sixth-order differentiation at the working wavelength of 1010 nm.

4. Results

To verify the edge extraction capability of the silicon hollow-cylinder metasurface's differential operation, we used input images with three vertical and horizontal stripes (see Figs. 4(a) and 4(i)). The intensity plots along the black dashed lines are shown in Figs. 4(e) and 4(m). The differential imaging results at the three resonant wavelengths are presented in Figs. 4(b)–4(d) and 4(j)–4(l), with insets showing magnified views of the framed regions. Figures 4(f)–4(h) and 4(n)–4(p) display the intensity distributions corresponding to the red, blue, and green dashed lines. At all three working wavelengths, the vertical and horizontal stripe edges are clearly captured, confirming the metasurface's broadband edge-detection ability. Notably, at 1340 nm, the first edge-line intensity distribution in Fig. 4(f) shows two closely spaced peaks at the edge. This typically represents the second-order differential process and aligns with the optical transfer function conclu-

sion in Fig. 3(a).

When the operating wavelength was set to 1140 nm, as shown in the magnified view of the blue boxed area in Fig. 4(c), multiple white fine stripes appeared at the edges. Figure 4(g) shows the first-edge-line intensity distribution, displaying four closely spaced peaks. This represents the typical characteristics of fourth-order differentiation and is consistent with our Fig. 3(b) conclusion on the fourth-order differential optical transfer function. At 1010 nm, the edges in Fig. 4(d) showed even more white fine stripes. The first edge-line intensity distribution in Fig. 4(h) revealed six closely spaced peaks, indicative of sixth-order differentiation, aligning with the Fig. 3(c) conclusion on the sixth-order differential optical transfer function. These phenomena were also observed in the vertical stripe outputs. In summary, our silicon hollow cylinder metasurface performed different-order high-order differential operations at 1340 nm, 1140 nm, and 1010 nm, achieving wavelength-division multiplexing. Here, we focus on the specific characteristics of three operating wavelengths: 1340 nm, 1140 nm, and 1010 nm. However, we have also calculated the optical transfer functions and image differentiation results for numerous other wavelengths, with details provided in the supplementary materials. This confirms that our metasurface can achieve high-performance high-order differential computation capabilities across nearly the entire broad operating range of 970 nm–1400 nm.

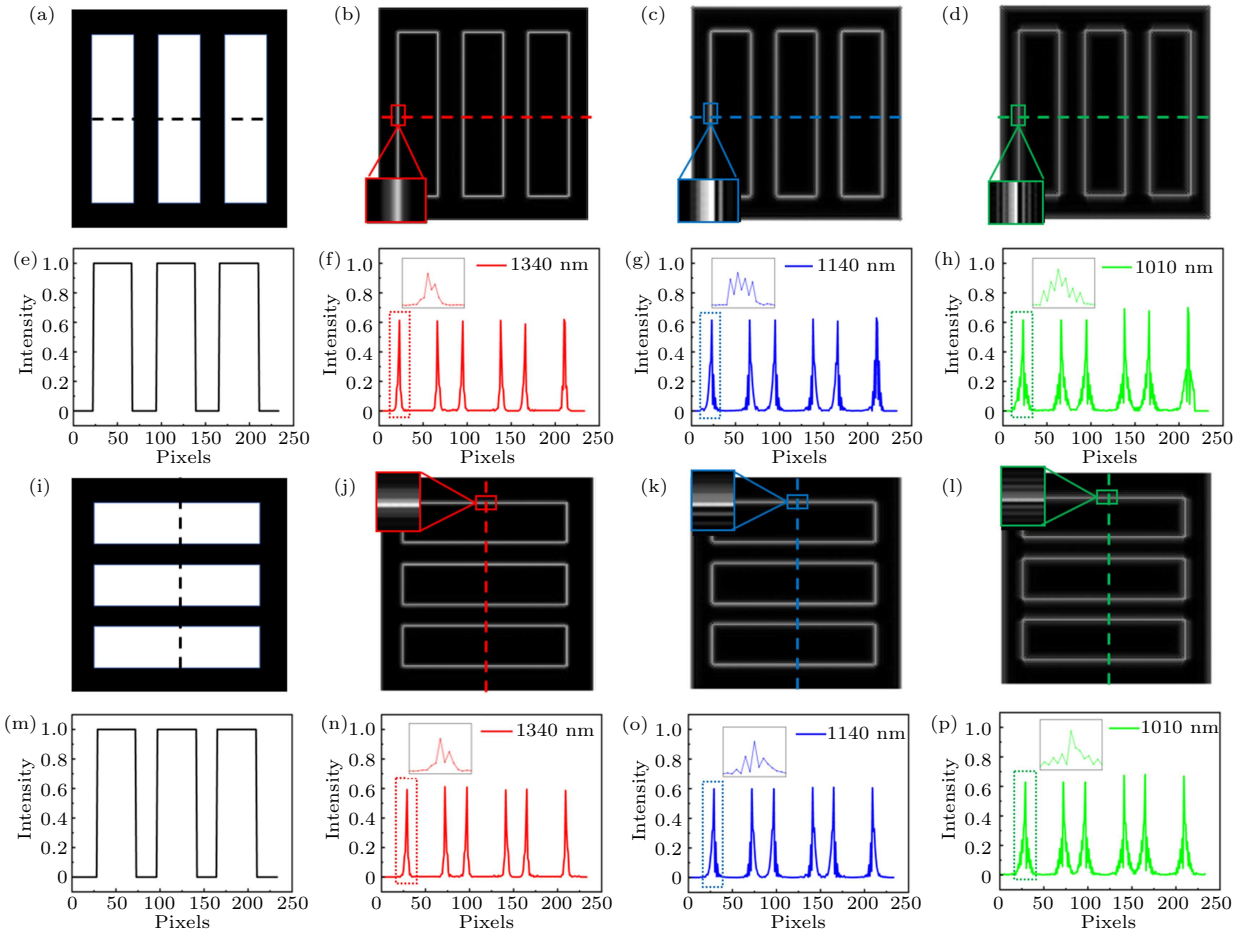


Fig. 4. Imaging results of differential computation at the resonant wavelengths of the silicon hollow-cylinder metasurface and the corresponding horizontal and vertical intensity distributions. (a), (e) Input images of three vertical stripes and intensity plots along the horizontal black dashed lines. (b)–(d), (f)–(h) Output images of vertical stripes and intensity plots along the horizontal red, blue, and green dashed lines at 1340 nm, 1140 nm, and 1010 nm. (i), (m) Input images of three horizontal stripes and intensity plots along the vertical black dashed lines. (j)–(l), (n)–(p) Output images of horizontal stripes and intensity plots along the vertical red, blue, and green dashed lines at 1340 nm, 1140 nm, and 1010 nm. Insets in (b)–(d), (j)–(l) show magnified views of the framed regions, and insets in panels (f)–(h), (n)–(p) show intensity distributions of the first edge lines.

To further validate the high performance of our silicon hollow-cylinder metasurface for 2D edge extraction, we input a complex 2D image of Nanjing University of Science and Technology's emblem (Fig. 5(a)). Featuring line, arc, and circular edges, this image serves as an effective testbed for evaluating the metasurface's processing capability. The output images obtained after processing by the metasurface at 1340 nm, 1140 nm, and 1010 nm (Figs. 5(b)–5(d)) exhibit clear, high-contrast edge details. All element edges are successfully extracted with uniformity, confirming the suitability of the metasurface's 2D optical transfer function for processing complex 2D structures (consistent with the characteristics presented in Figs. 3(e)–3(g)). Notably, the insets in Figs. 5(b)–5(d) reveal increasing edge stripe complexity at the character

"1953", which confirms that the metasurface implements distinct orders of differential operations at these three resonant wavelengths.

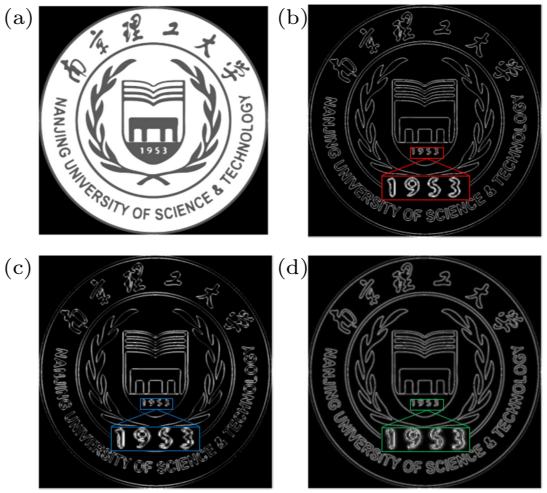


Fig. 5. (a) 2D input image of Nanjing University of Science and Technology's emblem. (b) Output image at 1340 nm. (c) Output image at 1140 nm. (d) Output image at 1010 nm. Insets in panels (b)–(d) show magnified views of the framed regions.

To the best of our knowledge, no one has previously proposed a metasurface that performs different-order differentiation using wavelength-division multiplexing. Spatial differentiation is one of the basic mathematical operations. Performing different-order differentiation with a single optical element is significant for optical analog signal processing. More crucially, the combination of multi-order differentiation enables a Taylor series expansion of the electromagnetic field. That is, optical analog computing may soon perform a Taylor series expansion of the input optical field's wave function.

Most of the previous work focused on second-order differentiation at single-wavelength or narrow spectral ranges and often overlooked the need for higher-order differentiation. By contrast, this work demonstrates second-order, fourth-order, and sixth-order 2D differentiations within a broad operational wavelength band from 970 nm to 1400 nm (spanning 430 nm). Here, we take the three wavelengths discussed above (1340 nm, 1140 nm, and 1010 nm) as examples. Detailed information on other wavelengths within the spectral range of 970 nm–1400 nm, as well as the correspondence between wavelengths and differential orders, can be found in the supplementary materials Fig. S1 and Table S1. Wavelength-division multiplexing (WDM) of higher-order differentiation is achieved. Specific data for each differentiation order are summarized in Table 1.

Table 1. Comparison between this work and others.

Ref.	Order of differentiation	Applicable wavelength	Resonance mode	NA
[37]	second order	1488.3 nm	quasi-BICs	0.08
[38]	second order	630 nm	ED	0.37
[30]	second order	1040–1088 nm (48 nm)	MD	0.5
[23]	second order	1100–1210 nm (110 nm)	TD	0.4
[9]	second order	1400–1600 nm (200 nm)	ED and MD	0.34
[35]	second order	1490 nm, 1560 nm	N.M.	0.34, 0.25
[39]	second order	652 nm, 689 nm	MD, ED	0.17
This work	second order	970–1400 nm (430 nm)	MD	0.71
	fourth order		EQD and MD	0.31
	sixth order		EQD	0.17

5. Conclusion

This study introduces a single-layer dielectric metasurface calculator based on wavelength division multiplexing. By tuning the resonance of silicon hollow cylinders, it performs multi-order optical differentiation in transmission mode. With a 430 nm bandwidth and a maximum NA of 0.7, it achieves second-, fourth-, and sixth-order differentiations at 1340 nm, 1140 nm, and 1010 nm, respectively. Multipole decomposition reveals that at shorter wavelengths (1010 nm), higher-order differentiation is dominated by electric quadrupole (EQD) resonance; at longer wavelengths (1340 nm), magnetic dipole (MD) resonance supports lower-order differentiation with low loss; and at mid-wavelengths (1140 nm), a hybrid EQD–MD resonance enables fourth-order differentiation. This wavelength-dependent behavior allows the device to dynamically switch differentiation orders via wavelength division multiplexing, overcoming the functional limitations of traditional metasurfaces. The metasurface also exhibits high-pass filtering within the incidence angle range. Its transmission and phase distributions closely match those of an ideal differentiator. It successfully extracts edges from vertical/horizontal stripes and complex 2D images. By integrating wavelength division multiplexing with multi-order differentiation in a single metasurface layer, this research paves the way for miniaturized and multifunctional optical computing systems, showing great potential in autonomous driving, biomedical imaging, and optical signal processing.

Acknowledgements

Project supported by the National Natural Science Foundation of China (Grant No. 11804161), the Open Research Fund of State Key Laboratory of Opto-Electronic Information Acquisition and Protection Technology (Grant No. OEIAPT202502), and the Fundamental Research Funds for the Central Universities (Grant Nos. 30923010907 and 2025201010).

References

[1] Chen C, Qi W, Yu Y and Zhang X L 2021 *Nanophotonics* **10** 2481
[2] Kazanskiy N L, Butt M A and Khonina S N 2022 *Nanomaterials (Basel)* **12** 2171
[3] Wang Z, Li T, Soman A, Mao D, Kananen T and Gu T 2019 *Nat. Commun.* **10** 3547
[4] Liu S K, Li Y H, Liu S L, Zhou Z Y, Li Y, Yang C, Guo G C and Shi B S 2020 *Opt. Express* **28** 35415
[5] Zhou J X, Qian H L, Chen C F, Zhao J X, Li G R, Wu Q Y, Luo H L, Wen S C and Liu Z W 2019 *Proc. Natl. Acad. Sci. USA* **116** 11137
[6] Chen Y, Yan D, Wang X, Qi T and Gao W 2024 *Opt. Express* **32** 24703
[7] Zhou J, Qian H, Zhao J, Tang M, Wu Q, Lei M, Luo H, Wen S, Chen S and Liu Z 2021 *Natl. Sci. Rev.* **8** nwaa176
[8] Zhang Y, Lin P, Huo P, Liu M, Ren Y, Zhang S, Zhou Q, Wang Y, Lu Y Q and Xu T 2023 *Nano Lett.* **23** 2991
[9] Komar A, Aoni R A, Xu L, Rahmani M, Miroshnichenko A E and Neshev D N 2021 *ACS Photonics* **8** 864
[10] Kim Y, Lee G Y, Sung J, Jang J and Lee B 2021 *Adv. Funct. Mater.* **32** 2106050
[11] Xie J T, Bie S H, Li M F, Yu Y J, Li Y F, Wang J G, Quan B G and Wu L A 2024 *Chin. Phys. B* **33** 104203
[12] Li Q Y, Liang M G, Liu S Q, Liu J W, Chen S Z, Wen S C and Luo H L 2025 *Opto-Electronic Advances* **8** 240239
[13] Silva A, Monticone F, Castaldi G, Galdi V, Alù A and Engheta N 2014 *Science* **343** 160
[14] Goodman J W 2005 *Introduction to Fourier Optics* (CO: Roberts & Company)
[15] Zhou Y, Chen R, Chen W, Chen R P and Ma Y 2020 *Opt. Commun.* **458** 124674
[16] Zangeneh-Nejad F, Khavasi A and Rejaei B 2018 *Opt. Commun.* **407** 338
[17] Zhu T, Zhou Y, Lou Y, Ye H, Qiu M, Ruan Z and Fan S 2017 *Nat. Commun.* **8** 15391
[18] Ruan Z 2015 *Opt. Lett.* **40** 601
[19] Zhang J, Ying Q and Ruan Z 2019 *Opt. Lett.* **44** 4511
[20] Zhu T F, Lou Y J, Zhou Y H, Zhang J H, Huang J Y, Li Y, Luo H L, Wen S C, Zhu S Y, Gong Q H, Qiu M and Ruan Z C 2019 *Phys. Rev. Appl.* **11** 034043
[21] Liu J W, Yang Q, Shou Y C, Chen S Z, Shu W X, Chen G, Wen S C and Luo H L 2024 *Phys. Rev. Lett.* **132** 043601
[22] Saba A, Tavakol M R, Karimi-Khoozani P and Khavasi A 2018 *IEEE Photon. Technol. Lett.* **30** 853
[23] Zhou C, Chen Y J, Li Y, Li J J, Zhao R Z, Tao C D, Liu C B, Bai Y, Li X, Wang Y T and Huang L L 2024 *Adv. Funct. Mater.* **34** 2313777
[24] Kwon H, Sounas D, Cordaro A, Polman A and Alu A 2018 *Phys. Rev. Lett.* **121** 173004
[25] Bezus E A, Doskolovich L L, Bykov D A and Soifer V A 2018 *Opt. Express* **26** 25156
[26] Wang H W, Guo C, Zhao Z X and Fan S H 2020 *ACS Photon.* **7** 338
[27] Zhou C, Zhao R Z, Li P J, Zhang Y, Chen Y J, Geng G Z, Li J J, Li X W, Wang Y T and Huang L L 2025 *Adv. Funct. Mater.* **35** 2426095
[28] Zhou Y, Zheng H Y, Kravchenko I I and Valentine J 2020 *Nat. Photon.* **14** 316
[29] Guo C, Xiao M, Minkov M, Shi Y and Fan S H 2018 *Optica* **5** 251
[30] Liu Y, Li X, Shi B, Jia Q, Zhang Y, Gao Y, Gao W, Sun F, Cao Y, Feng R and Ding W 2025 *Opt. Lett.* **50** 3517
[31] Zhou J X, Liu S K, Qian H L, Li Y H, Luo H L, Wen S C, Zhou Z Y, Guo G C, Shi B S and Liu Z W 2020 *Sci. Adv.* **6** eabc4385
[32] Ma H Q, Han Y X, Dou T Q and Li P Y 2023 *Chin. Phys. B* **32** 020304
[33] Bai S K, Xiang Y J and Zhang Z X 2023 *Chin. Phys. B* **32** 024209
[34] Babicheva V E and Evlyukhin A B 2018 *ACS Photon.* **5** 2022
[35] Cotrufo M, Singh S, Arora A, Majewski A and Alu A 2023 *Optica* **10** 1331
[36] Zhou Y, Chen R, Chen W J and Ma Y G 2020 *Acta Phys. Sin.* **69** 157803 (in Chinese)
[37] Liu T, Qiu J, Xu L, Qin M, Wan L, Yu T, Liu Q, Huang L and Xiao S 2024 *Nano Lett.* **24** 14466
[38] Wan L, Pan D, Yang S, Zhang W, Potapov A A, Wu X, Liu W, Feng T and Li Z 2020 *Opt. Lett.* **45** 2070
[39] Liu T T, Qiu J M, Yu T B, Liu Q G, Li J and Xiao S Y 2025 *Appl. Phys. Lett.* **126** 081702